

A Stabilized Finite Element Analysis for Three-Dimensional Czochralski Silicon Melt Flow

Ville Savolainen, Jari Järvinen, Juha Ruokolainen* and Olli Anttila†

Abstract

We have applied stabilized finite element method for the silicon melt flow in Czochralski crystal growth. The finite element formulation and the simulation results for transient melt flow in a cylindrically symmetric and in a three-dimensional model of a large-scale crystal growth environment are presented.

1 Introduction

1.1 Czochralski Crystal Growth

Electronics industry is the largest and the fastest growing manufacturing industry in the world. The semiconductor industry provides the basis for the rapid development of the various electronics applications.

Silicon, produced as silicon wafers (Fig. 1), is the strategic material for the semiconductor industry. The wafers, subject to very stringent quality requirements, are cut and processed from single silicon crystals. The Czochralski (CZ) method, illustrated schematically in Fig. 2, is the most frequently used single crystal growth technique for silicon. More than 95% of all silicon wafers are made from the crystals grown by the CZ method.

In the Czochralski method, purified polysilicon pellets or nuggets are first melted in a heated high purity quartz crucible at above 1400°C in a low-pressure argon atmosphere. After reaching the desired initial temperature and process conditions, crystal growth is initiated by dipping a small seed crystal into the melt. A cylindrical single crystal is then pulled vertically from the melt in such a way that it grows with a constant diameter except during the initial and final stages of the growth (Fig. 3). This requires that, e.g., the pulling velocity and/or the heating power are carefully controlled during the growth process. In addition, the crystal rod and the crucible are usually rotated in opposite directions.

*Ville.Savolainen@csc.fi, Jari.Jarvinen@csc.fi and Juha.Ruokolainen@csc.fi, Center for Scientific Computing, P.O. Box 405, FIN-02101 Espoo

†Olli.Anttila@okmetic.com, Okmetic Ltd., Sinimäentie 12, FIN-02631 Espoo

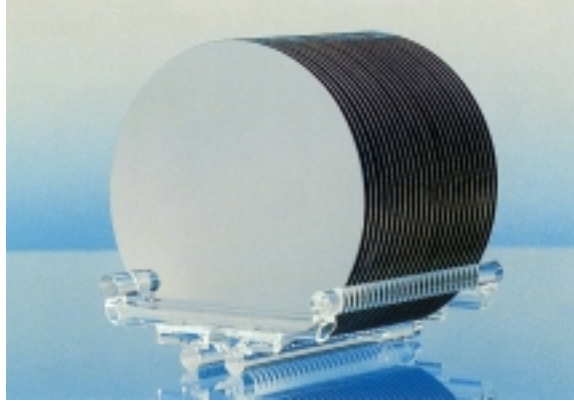


Figure 1: Industrially produced silicon wafers

1.2 Modeling and Simulation

In the Czochralski process, the couplings between different physical phenomena lead to quite a complicated behavior of the system. Inside the Czochralski furnace, heat is transferred by radiation between the various surfaces, by convection in the silicon melt and argon, and conduction everywhere. Radiation dominates the overall heat transfer due to the high temperature environment. Heat transfer in the melt flow is dominated by convection. Forced, natural and, to a lesser extent thermocapillary, convection mechanisms drive the melt flow.

We (the authors and Jussi Heikonen at CSC) have modeled various aspects of the CZ system, including heat transfer in the system, melt and gas flow, and the magnetic Czochralski growth (MCZ), where the crystal growth is controlled by an external magnetic field. Fig. 4 depicts a simplified axisymmetric model of the CZ furnace. In addition, chemical reactions, e.g., the evaporation of the silicon monoxide, take place during the process and could be modeled. In this paper, we concentrate on the simulation of the melt flow, which is the computationally most intensive part of the system to model.

Temperature and the melt flow fluctuations during the growth reduce the homogeneity of the crystal. The crystal defects and undesired impurities can make the wafers unacceptable for IC manufacture. Thus, one of the goals in the crystal growing process development is to avoid, or at least dampen, these fluctuations. The benefits will be twofold: (1) the material homogeneity will be improved, giving better yields in the IC production, and (2) the losses of the single crystalline structure, the worst-case result of uncontrolled fluctuations, will be reduced. Our simulations exhibit these fluctuating patterns in the melt. The ultimate goal of the modeling is to optimize the process parameters to dampen the fluctuations.

The growth of a single silicon crystal by the Czochralski method lasts normally 30-50 hours. Although the process itself is rather slow, there are phenomena with much shorter time scales. For instance, one can observe fluctuations

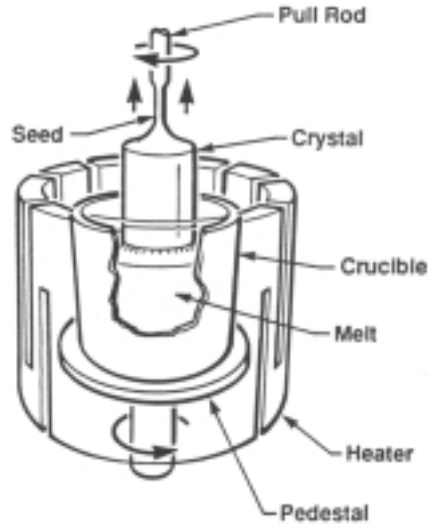


Figure 2: A schematic configuration of Czochralski crystal growth, [1].

in crystal properties with a characteristic period corresponding to a few dozens of seconds of the growth process. These fluctuations reflect the quasi-periodic nature of the melt flow field.

The economics of the production of silicon crystals depends on the growth yields, raw materials consumption as well as on process times. In addition, the microdefect structure of the crystals, influenced by several process variables, has to be controlled to guarantee the high quality of the wafers. If everything in the process development is made experimentally, considerable time and money has to be invested. Furthermore, experimental measurements are typically very laborious and require construction of complicated experimental systems ([2]) as well as further economical investments.

At the same time powerful computers—based on silicon technology—and numerical algorithms have evolved to the point where very large and complex numerical simulations can be carried out in a sufficiently short time frame. These simulations provide new insight into the physical phenomena in the crystal growth, and reduce the economical investments required in the experimental work. Experimental methods cannot, however, be omitted. They offer invaluable information from physical mechanisms. Furthermore, they form a basis for validating the numerical results and provide necessary input data for simulations.

Modeling and numerical simulation of Czochralski silicon crystal growth has been under an active research worldwide. Several research groups have reported about the simulation of global temperature distribution in axisymmetric Czochralski geometry, [3]-[4]. In these studies, the silicon melt flow has been

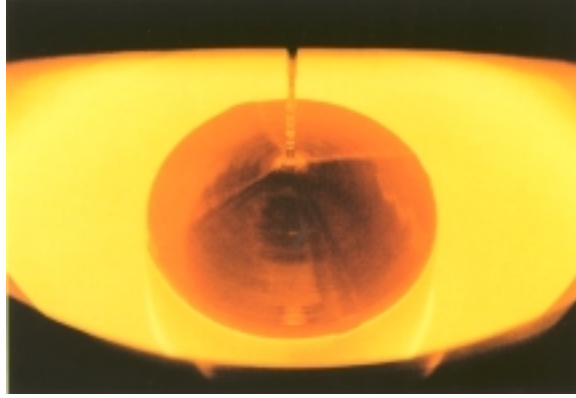


Figure 3: Initial stage of Czochralski crystal growth

approximated either by an enhanced effective thermal conductivity or by using reduced Reynolds numbers.

Melt flow in Czochralski growth has been studied in detail in [5]-[8]. In [5], the authors study oscillatory convection in a low aspect ratio Czochralski melt geometry. They neglect the surface tension forces and crucible and crystal rotations, and consider heat transfer at the melt-gas interface with the idealized radiation boundary condition. The numerical method is based on the control volume integral approach.

In [6], Ryckmans et al. consider the influence of melt convection on global heat transfer and melt-crystal interface shape. Their analysis is based on axisymmetric global temperature distribution and melt convection. They use Galerkin formulation, reporting about convergence problems in solving Navier-Stokes equations with high Grashof and Reynolds numbers.

In [7] and [8] the authors present three-dimensional melt flow computations. In [7], Kakimoto et al. utilize axisymmetric global temperature distribution at the melt-gas interface. Their computation is based on control volume method (FLUENT), and they simulate melt convection in a small-scale crucible with modest crucible rotation rates. In [8], Xiao and Derby concentrate on time-dependent melt flow in Czochralski oxide growth. Their numerical simulation tool is based on the Galerkin finite element method.

1.3 Research Objective: Simulation of Large Scale Silicon Melt Flow

Diameter of single silicon crystals produced industrially by the Czochralski method are typically in the range of 100 to 200 mm. The trend towards larger diameters is evident in the future, 300 mm diameter crystals being already in pilot production. In large-scale CZ silicon crystal growth environment, the melt flow exhibits complex three-dimensional, transient and quasi-periodic features,

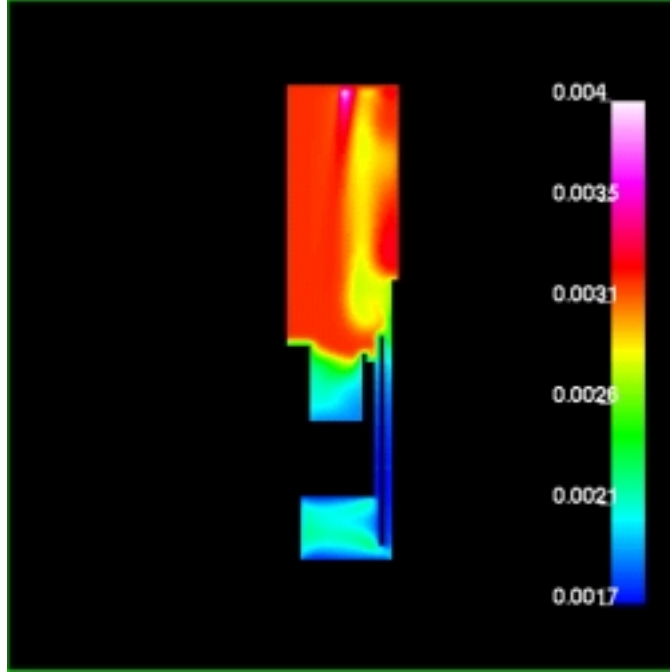


Figure 4: “Global” CZ model (crucible, melt and crystal shown in black).

which are reflected in the incorporation rate of intrinsic point defect densities to the crystal. Thus, the melt flow plays an essential role in the crystal quality. Consequently, it is important to simulate the melt flow in a real crystal growth geometry and by using real material parameters.

As reported, attempts to model silicon melt flow by the Galerkin method have repeatedly led to loss of convergence, [1], [6] and [9]. Our earlier simulations in the realistic CZ geometry reported in [12] have also been carried with a reduced density in order to achieve convergence.

In this work, we have applied stabilized finite element method for the silicon melt flow in CZ crystal growth. We will present the finite element formulation and the simulation results for transient melt flow in cylindrically symmetric and three-dimensional models of a realistic geometry of a large-scale crystal growth environment.

We have solved the cylindrically symmetric problem with realistic material and process parameters. The cylindrical symmetry may, however, be artificially forced by the model, and it is known to be broken in the large-scale CZ silicon growth. We have solved the three-dimensional model with melt density reduced by a factor of 10 from the value for silicon, our aim being to trace the critical Reynolds and Grashof numbers for the transition to the three-dimensional flow.

2 Mathematical Model

We will consider the silicon melt flow and heat transfer in melt regions Ω and $\bar{\Omega}$ with Grashof, forced and Marangoni convections.

The two problem formulations differ so that in Ω we assume *a priori* cylindrical symmetry, i.e., all partial derivatives with respect to the azimuthal coordinate vanish. In this case, the model is solved in cylindrical coordinate system. Furthermore, the solver is written in curvilinear tensor formulation, implicating that the velocity solution is obtained and the boundary conditions are set for the contravariant components (v^r, v^ϕ, v^z) .

In the second formulation, the region $\bar{\Omega}$ is obtained by rotating Ω around the z -axis. The problem is solved in a truly three-dimensional form in the Cartesian coordinate system (x, y, z) .

Both cases are formulated and solved in time-dependent form. In both cases, the same partial differential equations with the same physical boundary conditions are solved with the same stabilized finite element method.

2.1 Transport Equations

The flow is governed by the incompressible Navier-Stokes equations

$$\nabla \cdot \vec{v} = 0, \quad (1)$$

$$\rho \left(\frac{\partial \vec{v}}{\partial t} + \vec{v} \cdot \nabla \vec{v} \right) = \nabla \cdot \boldsymbol{\sigma} + \vec{f}, \quad (2)$$

with Newtonian stress tensor

$$\boldsymbol{\sigma} = -p\mathbf{I} + \boldsymbol{\tau} = -p\mathbf{I} + 2\mu\boldsymbol{\epsilon}$$

and linear strain-rate tensor $\boldsymbol{\epsilon}$, written in the contravariant form as

$$\epsilon^{ij} = \frac{1}{2} (g^{jk} v^i_{,k} + g^{ik} v^j_{,k}).$$

The gravitational force is described by the Boussinesq approximation

$$\vec{f} = \rho_0 \beta (T - T_0) g \vec{e}_z,$$

where the constant potential caused by the reference density shifts the pressure solution. In other terms of the Navier-Stokes and heat equation, $\rho = \rho_0$ is used according to the Boussinesq approximation.

The heat flow is governed by the energy equation for incompressible fluid

$$\rho c_p \left(\frac{\partial T}{\partial t} + \vec{v} \cdot \nabla T \right) = -\nabla \cdot \vec{q}, \quad (3)$$

where we have ignored the viscous heating. We have used the scalar Fourier's law

$$\vec{q} = -k \nabla T$$

for the heat flux. There are no volume sources.

2.2 Boundary Conditions

The only formal difference between the boundary conditions on Γ_i for Ω and on $\bar{\Gamma}_i$ for $\bar{\Omega}$ is that the symmetry axis does not exist as a boundary for the three-dimensional model. Thus, no symmetry boundary conditions are specified there.

We will present the boundary conditions on Γ_i in the form appropriate for the cylindrically symmetric model. The change of variables to the three-dimensional Cartesian system is made easily; the boundary conditions themselves are cylindrically symmetric on $\bar{\Gamma}_1$, $\bar{\Gamma}_2$ and $\bar{\Gamma}_3$.

On Γ_1 , the crucible wall, we have no-slip conditions for the velocity

$$v^r = v^z = 0, v^\phi = \omega_1,$$

and time-independent Dirichlet boundary condition for the temperature

$$T = T_w(\vec{x}).$$

On Γ_2 , the melt surface adjacent to the gas, the normal component of the velocity vanishes

$$v^z = 0,$$

the surface tension γ is approximated by the linear relation

$$\gamma = \gamma_0(1 - \vartheta(T - T_0)),$$

leading to the tangential boundary stress

$$\boldsymbol{\sigma} \cdot \vec{e}_r = -\gamma_0 \vartheta \frac{\partial T}{\partial r} \vec{e}_r.$$

The heat flux is described by the idealized radiation

$$\vec{q} \cdot \vec{e}_z = \sigma \varepsilon (T^4 - T_{ext}^4).$$

On Γ_3 , the melt surface adjacent to the crystal, we have no-slip conditions for the velocity

$$v^r = v^z = 0, v^\phi = \omega_3,$$

and the temperature is at the melting point temperature

$$T = T_m.$$

On Γ_4 , the symmetry axis,

$$v^r = 0.$$

The degrees of freedom left free on Γ_2 , $\bar{\Gamma}_2$ and Γ_4 will receive the natural boundary conditions of the variational form.

Reference density	$\rho_0 = 2490 \text{ kg/m}^3$
Viscosity	$\mu = 7.5 \cdot 10^{-4} \text{ kg/m}^3$
Coefficient of thermal expansion	$\beta = 1.4 \cdot 10^{-4} \text{ 1/K}$
Reference temperature	$T_0 = 1683 \text{ K}$
Heat capacity	$c_p = 1000 \text{ J/kgK}$
Heat conductivity	$k = 64 \text{ W/mK}$
Emissivity	$\varepsilon = 0.3$
External temperature	$T_{ext} = 1600 \text{ K}$
Melting point temperature	$T_m = 1685 \text{ K}$
Crucible wall temperature	$T_w(\vec{x}) \equiv 1715 \text{ K}$
Surface tension	$\gamma_0 = 0.72 \text{ N/m}$
Thermocapillary coefficient	$\vartheta = 10^{-4}$
Crucible rotation rate	$\omega_1 = -\pi/6 \text{ 1/s}$
Crystal rotation rate	$\omega_3 = 2\pi/3 \text{ 1/s}$
Gravitational acceleration	$g = 9.81 \text{ m/s}^2$
Stefan-Boltzmann constant	$\sigma = 5.6697 \cdot 10^{-8} \text{ J/m}^2\text{sK}^4$

Table 1: Material parameters and other constants

2.3 Material Parameters

The values of the material parameters used for the melt, boundary conditions and physical constants are listed in Table 1. In the three-dimensional model we have, however, used a reduced value $\rho' = \rho/10$ for the melt density in order to keep the problem size and solution time required to achieve convergence for the Navier-Stokes equations reasonable. The value of the external temperature, i.e., characterizing the thermal environment that is not modeled, is set so that it gives a fairly reasonable temperature distribution on the melt surface.

We solve the transport equations without a turbulence model, in laminar form. With the realistic material parameters, the flow is probably mildly turbulent. However, stabilized FEM with adequately refined quadratic elements reaches a converged solution on each time step.

3 Numerical Methods

3.1 Linearization

Our FEM formulation is to solve Eqs. 1 and 2 strongly coupled, *i.e.*, to assemble a single linearized system of equations for the nodal values of (\vec{v}, p) , but to solve this subsystem weakly coupled with Eq. 3. Therefore, in Navier-Stokes equations we need to linearize the convection term and in the energy equation the idealized radiation term. We use Picard linearization for the convection term

$$\vec{v} \cdot \nabla \vec{v} = \vec{\mathcal{V}} \cdot \nabla \vec{v},$$

and the following linearization for the radiation term

$$\sigma\varepsilon (T^4 - T_{ext}^4) = \sigma\varepsilon (\mathcal{T}^3 + \mathcal{T}^2 T_{ext} + \mathcal{T} T_{ext}^2 + T_{ext}^3) (T - T_{ext}).$$

Here the symbols $\vec{\mathcal{V}}$ and \mathcal{T} refer to the values from the previous nonlinear iteration. The Newton's linearization is less stable, especially for the Navier-Stokes equations.

3.2 Discretization and Stabilization

We use the following stabilized variational formulation given in [10] and [11].

Denoting the residual of Eq. 3 by

$$R(T) = \rho c_p \left(\frac{\partial T}{\partial t} + \vec{v} \cdot \nabla T \right) - \nabla \cdot (k \nabla T),$$

the variational form is

$$B(T, \Psi) = \langle R(T), \Psi \rangle + \sum_e \langle R(T), \tau W(\Psi) \rangle,$$

where the diffusion term in the first inner product is integrated by parts. The functions Ψ , which are also used as the interpolation functions for T , are the basis functions for the elements. We use the Galerkin Least-Squares method (GLS) with

$$W = \vec{v} \cdot \nabla \Psi - \nabla \cdot (k \nabla \Psi),$$

and elementwise stabilization parameters

$$\begin{aligned} \tau &= \frac{h_K}{2 \|\vec{v}\|} \min(1, \text{Pe}_K(x)), \\ \text{Pe}_K(x) &= \frac{m_K h_K \|\vec{v}\|}{2k}. \end{aligned}$$

The parameter h_K is determined by the size of the element and the parameter m_K by the element basis functions.

We denote the residual of the linearized form of Eq. 2 by

$$\vec{R}_m(\vec{v}, p) = \rho_0 \left(\frac{\partial \vec{v}}{\partial t} + \vec{\mathcal{V}} \cdot \nabla \vec{v} \right) - \nabla \cdot \boldsymbol{\sigma} - \vec{f},$$

the residual of Eq. 1 by

$$R_c(\vec{v}) = \nabla \cdot \vec{v},$$

and combine these to the residual of the Navier-Stokes equations

$$\vec{R}(\vec{v}, p) = (\vec{R}_m(\vec{v}, p), R_c(\vec{v})).$$

The variational form of this is

$$\mathbf{B}((\vec{v}, p), \vec{\Psi}) = \langle \vec{R}(\vec{v}, p), \vec{\Psi} \rangle + \sum_e \langle (\vec{R}_m(\vec{v}, p), 0), \tau \vec{W}(\vec{\Psi}) \rangle,$$

where the divergence of the stress tensor in the first term is integrated by parts. The continuity equation gives an additional term

$$\sum_e \langle (\vec{0}, R_c(\vec{v}, p), (\vec{0}, \delta(\vec{0}, W_c(\Psi_c))) \rangle.$$

Writing the stabilization contribution to the weight functions as

$$\vec{W} = (\vec{W}_m, W_c),$$

we use the GLS method for the Navier-Stokes equations as well:

$$\vec{W} = \rho_0 \vec{\mathcal{V}} \cdot \nabla \vec{\Psi}_m - \mu \nabla^2 \vec{\Psi}_m,$$

$$W_c = -\nabla \Psi_c.$$

All the components of $\vec{\Psi}_m$ and Ψ_c belong to the same interpolation functions as Ψ . The stabilization parameters are

$$\begin{aligned} \tau &= \frac{h_K}{2\rho_0 \|\vec{\mathcal{V}}\|} \min(1, \text{Re}_K(x)), \\ \delta &= \rho_0 h_K \|\vec{\mathcal{V}}\| \min(1, \text{Re}_K(x)), \\ \text{Re}_K(x) &= \frac{\rho_0 m_K h_K \|\vec{\mathcal{V}}\|}{4\mu}. \end{aligned}$$

The parameter m_K depends on the type of the element and h_K on its size [11].

These variational forms lead to two linearized systems of ordinary differential equations:

$$M \frac{\partial \vec{T}}{\partial t} + A \vec{T} = \vec{F},$$

$$N \frac{\partial \vec{q}}{\partial t} + D \vec{q} = \vec{G},$$

where \vec{q} consists of the nodal values of the velocity components and pressure.

3.3 Elements

We have used quadratic elements for both the cylindrically symmetric and the three-dimensional model for the final values of the material parameters. In both cases, unstructured mesh is refined under the crystal and near the symmetry

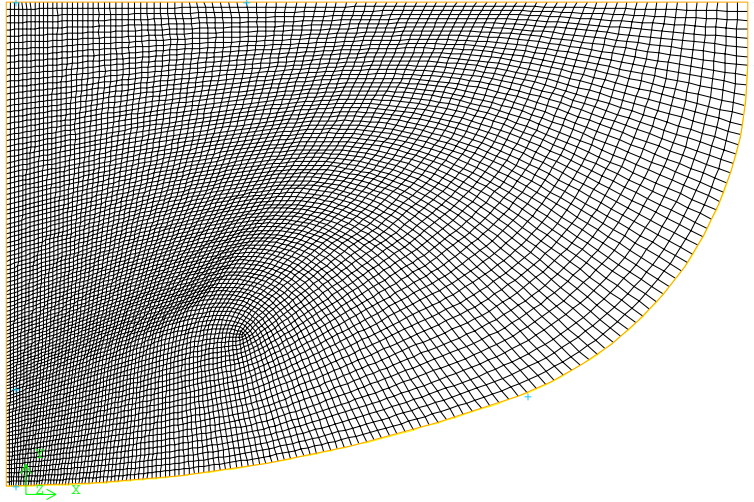


Figure 5: Quadratic elements mesh for the cylindrically symmetric model

axis in order to capture the flow complexity and yet to keep the overall number of elements reasonable as shown in Figs. 5 and 6.

The cylindrically symmetric model consists of 3573 9-node quadrilateral bulk elements and 208 3-node line elements. The total number of nodes is 14501.

In the three-dimensional model there are 112861 10-node tetrahedral bulk elements and 9766 6-node triangles on the boundaries. The total number of nodes is 160403.

Initially, we tried to solve the models with linear elements. They, however, failed to yield converged results, as material and process parameters were increased. When similar density of nodes with quadratic elements was used, the

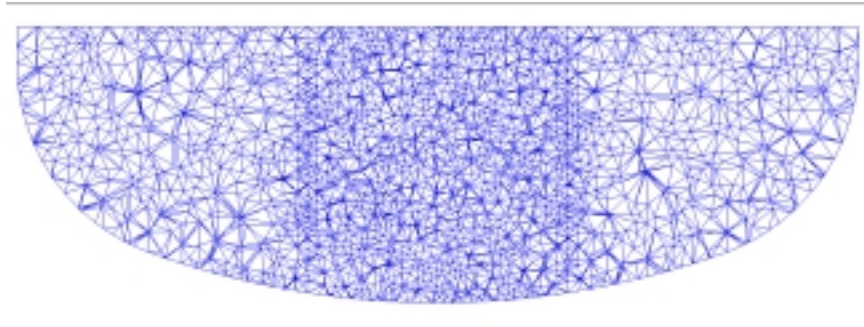


Figure 6: Quadratic tetrahedral mesh cut at the plane $x = 0$.

models suffered no convergence problems. This may also reflect the fact that the change from quadratic to linear elements changes the stabilization method from GLS to SUPG.

All results shown for the cylindrically symmetric model are calculated by the quadratic elements. For the three-dimensional model we did not, however, recalculate the results for the first 99 seconds, but those are obtained by the linear tetrahedral elements. By using a shorter time-step, we are able to achieve converged results until that point. The results were then interpolated to the quadratic mesh.

3.4 Time Integration

The time integration is done by the implicit Euler method (take $\theta = 0$ in the following equations), i.e., in the energy equation by

$$\left[\frac{1}{\Delta t} M + (1 - \theta) A_i^{k-1} \right] \vec{T}_i^k = \frac{1}{\Delta t} M \vec{T}_{i-1} - \theta A_{i-1} \vec{T}_{i-1} + \theta \vec{F}_{i-1} + (1 - \theta) \vec{F}_i^{k-1}.$$

and in the Navier-Stokes equations by

$$\left[\frac{1}{\Delta t} N + (1 - \theta) D_i^{k-1} \right] \vec{q}_i^k = \frac{1}{\Delta t} N \vec{q}_{i-1} - \theta D_{i-1} \vec{q}_{i-1} + \theta \vec{G}_{i-1} + (1 - \theta) \vec{G}_i^{k-1}.$$

In the three-dimensional model, we switched the time integration method to the second order BDF method between $t = 135 \dots 150$ s, as it sometimes may produce slightly less diffuse (more accurate) results. BDF-2 method is also an implicit scheme, given by

$$\vec{y}_k = 4/3 \vec{y}_{k-1} - 1/3 \vec{y}_{k-2} + 2h/3 \vec{f}_k.$$

It is straightforward to apply BDF methods to our finite element model, e.g., for the energy equation we obtain:

$$\left[M + \frac{2}{3} \Delta t A_i^{k-1} \right] \vec{T}_i^k = M \left(\frac{4}{3} \vec{T}_{i-1} - \frac{1}{3} \vec{T}_{i-2} \right) + \frac{2}{3} \Delta t \vec{F}_i.$$

3.5 Solution of the Linear Systems

Having chosen the time integration method, we have two systems of linear equations. In the following, we denote one of these generically by $A \vec{x} = \vec{b}$. The matrix A represents now the bracketed quantity above, the vector \vec{b} the whole right-hand side of the system, and the vector \vec{x} the unknowns.

For the realistic value of the density, all iterative methods and preconditioners we have tried, fail to converge. Therefore, in the cylindrically symmetric model, we were forced to use more time and memory consuming direct solver for both linearized systems of equations. This is implemented in ELMER, the FEM solver we have used, by calling the LAPACK routines for band matrices

to compute the LU factorization and solve the system. The bandwidths of the systems are optimized by the Reverse Cuthill-McKee algorithm.

When the density is reduced by the factor of ten, iterative solvers still work. Thus, the BiCGStab method with the ILU preconditioning is used in the three-dimensional model for both linear systems. Especially for the Navier-Stokes equations that have 641 612 unknowns, this saves a lot of CPU time. Convergence criteria for the iterative method was set to

$$\frac{\|A\vec{x} - \vec{b}\|_2}{\|A\|_F\|\vec{x}\|_2 + \|\vec{b}\|_2} \leq 10^{-6}.$$

The iterative method library HUTIter developed by Jouni Malinen (CSC and the Helsinki University of Technology) is used in ELMER.

3.6 Solution of the Non-Linear Systems

The convergence criteria for the non-linear iterations is

$$\frac{\|\vec{x}^{k+1} - \vec{x}^k\|_2}{\|\vec{x}^{k+1}\|_2} \leq \varepsilon_x$$

where $\varepsilon_T = 10^{-6}$ and $\varepsilon_v = 10^{-4}$. After some experimentation, an effective iteration strategy was deemed to take alternating Navier-Stokes and temperature iterations. In addition, the Navier-Stokes iteration is updated with the relaxation parameter λ taking values between 0.5 and 0.7.

$$\vec{q}^{k+1} := \lambda \vec{q}^{k+1} + (1 - \lambda) \vec{q}^k.$$

3.7 Time Integration Strategy

We have used the initial conditions

$$v^r = 10^{-6} \text{ m/s}, v^z = 0, v^\phi = 0, T = 1715 \text{ K}$$

at $t = 0$ in Ω .

The time step Δt was taken as 1.0 s in both models, when quadratic elements were used. We have done some experiments with shorter and longer time steps, and $\Delta t = 1.0$ s was deemed an adequate choice. For the linear elements, however, progressively shorter time steps were required and used (down to 0.25 s between $t = 70 \dots 100$ s) as the flow complexity increased.

In addition, we started simulations for both models with the melt density reduced to 1% of the true value, increasing it to the final values ρ and $\rho' = \rho/10$ during the first 50 seconds.

Both simulations are run for 150 s.

Cylindrically symmetric model	$v_{\perp} = \sqrt{(v^r)^2 + (v^z)^2}$ T
3-d model	$\ \vec{v}\ = \sqrt{(v_x)^2 + (v_y)^2}$ on the surface T on the surface v_z on $x = 0$ T on $x = 0$

Table 2: Video animations, [13].

3.8 Software and Hardware for the Simulation Runs

The mathematical model was implemented in and results calculated by ELMER, a general-purpose FEM software package written at CSC. Among several other partial differential equations, physical models and numerical methods, the stabilized finite element formulation of the coupled incompressible flow described above is a part of the standard ELMER package. The ELMER Solver is written mainly in Fortran 90, and is available in Unix (SGI, DEC and Linux) and Windows NT environments.

The simulations were run on CSC's COMPAQ AlphaServer GS140 work station Caper (`caper.csc.fi`) on a single 525 MHz EV6 processor.

Postprocessing is done by ELMER Post, part of the ELMER package. Meshes are generated by the commercial preprocessor GAMBIT.

3.9 Results

The simulation results were presented on a video in the minisymposium, [13]. Table 2 lists the temperature and velocity distributions shown in the animation.

The time integration strategy leads in both cases to an initial spin-up period of almost 100 seconds before a physically meaningful solution to the problem is reached. In the cylindrically symmetric case, the quasi-periodic solution has formed between $t = 80 \dots 150$ s. The length of a period is about 20 seconds. In the three-dimensional model, the flow pattern approaches nearly a symmetric and steady-state solution between $t = 100 \dots 150$ s.

The temperature distribution in the cylindrically symmetric model at the moment $t = 150$ s is shown in Fig. 7. The natural and forced convections combine to form the time-dependent wavy temperature isotherms.

The absolute velocity without the azimuthal component $v_{\perp} = \sqrt{(v^r)^2 + (v^z)^2}$ at the same moment is shown in Fig. 8. The axisymmetric convective cells follow the quasi-periodic temperature isotherms. The fine-scale structure of flow can perhaps be seen better here than in the temperature field. There is a quasi-periodic pump on the symmetry axis mixing effectively the flow. Even some of the individual rolls, e.g., the ones near the crucible wall, seem to rise periodically. The strongest rolls are concentrated below the crystal and near the crucible boundaries. The maximum values of v_{\perp} are about 5 cm/s, except on the symmetry axis pump about 10 cm/s.

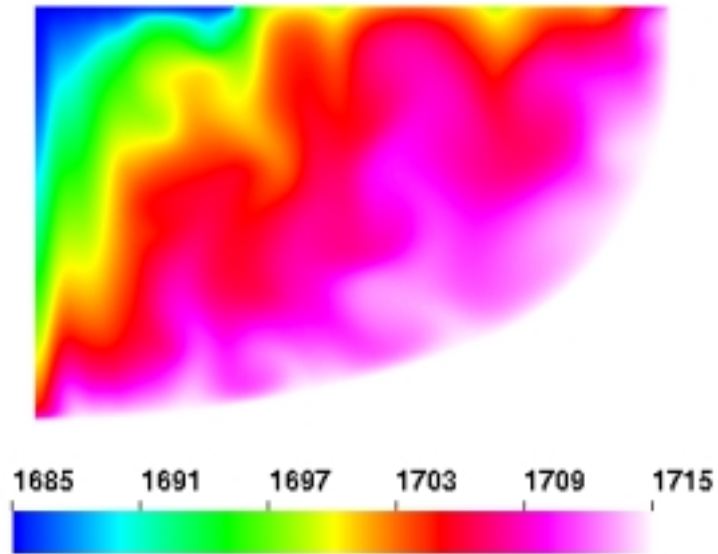


Figure 7: Temperature field at $t = 150$ s

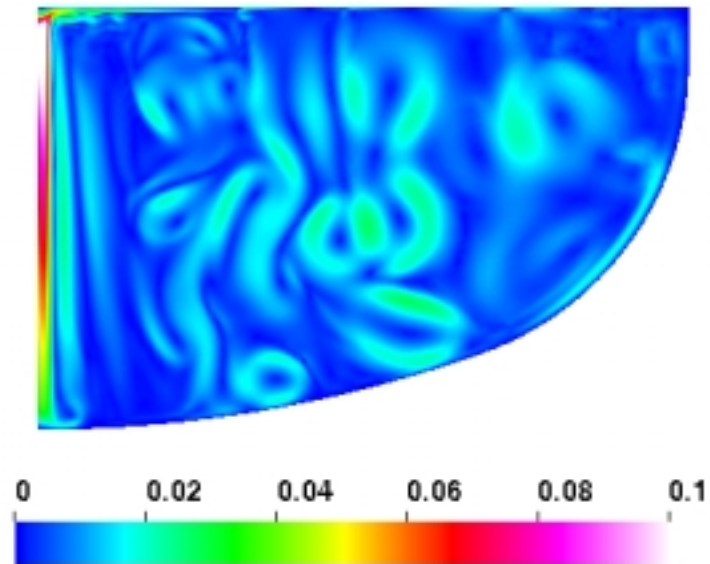


Figure 8: Perpendicular velocity field v_{\perp} at $t = 150$ s

The azimuthal velocity rv^ϕ at $t = 150$ s is depicted in Fig. 9. Generally, the azimuthal component follows the rotation of the crucible. The influence of the crystal rotation can be seen in a very thin region below the crystal. The convective rolls also transport higher or lower azimuthal velocity from outer or inner radial directions, respectively.

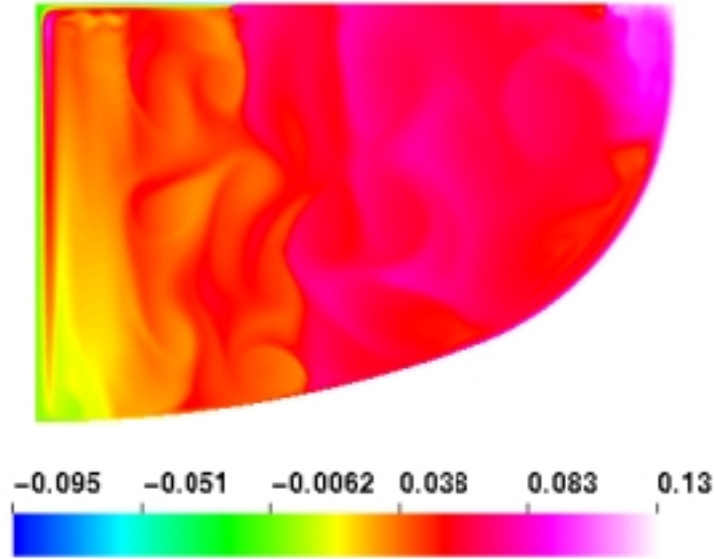


Figure 9: Azimuthal velocity field rv^ϕ at $t = 150$ s

For the three-dimensional case, Figs. 10–13 show the temperature and velocity distributions from the melt surface and the plane $x = 0$ at $t = 150$ s. The flow approaches a more symmetric and nearly a steady-state solution. The size and the number of convection rolls is smaller, since natural convection is much weaker with the reduced density. There is a slightly asymmetric rotating structure on the melt surface that has not yet been damped out. Marangoni force and the radiative cooling on the melt surface are perhaps misguidingly strong as they are not reduced in the same ratio by factor of ten as Grashof convection is.

4 Conclusions

Exact characterization of silicon melt flow, either experimentally or numerically, is a most challenging task. A direct experimental measurement of flow velocities requires a complicated X-ray radiography system. Even the X-ray measurements are applicable only to small-scale crucibles.

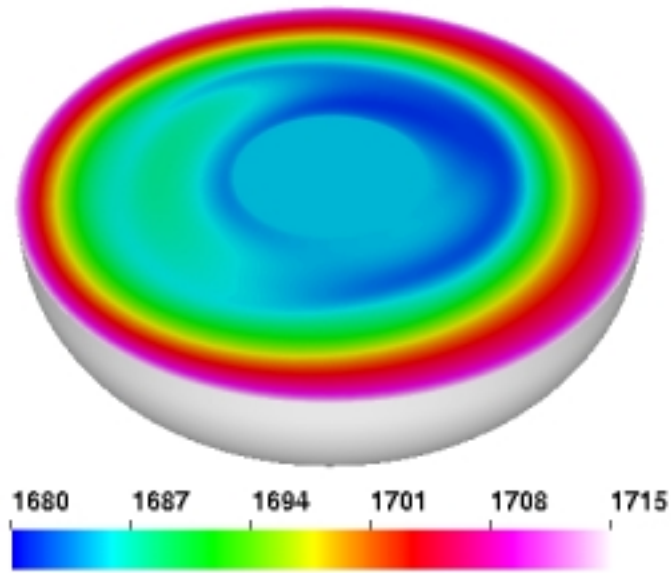


Figure 10: Surface temperature at $t = 150$ s

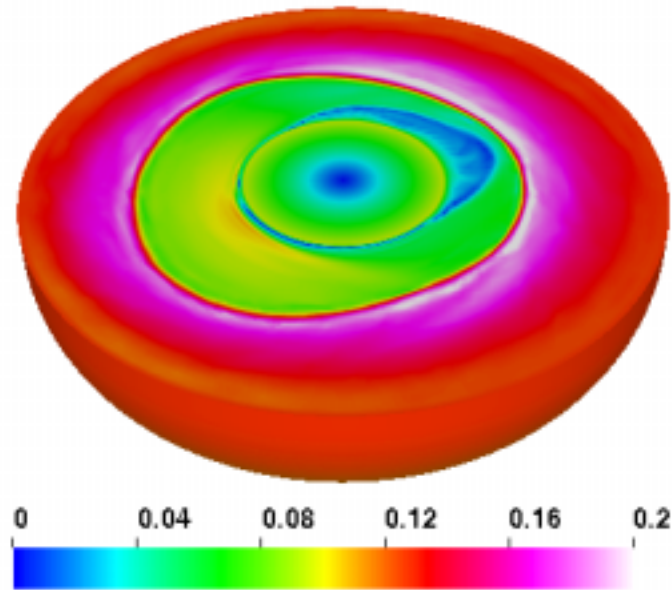


Figure 11: Velocity field at $t = 150$ s

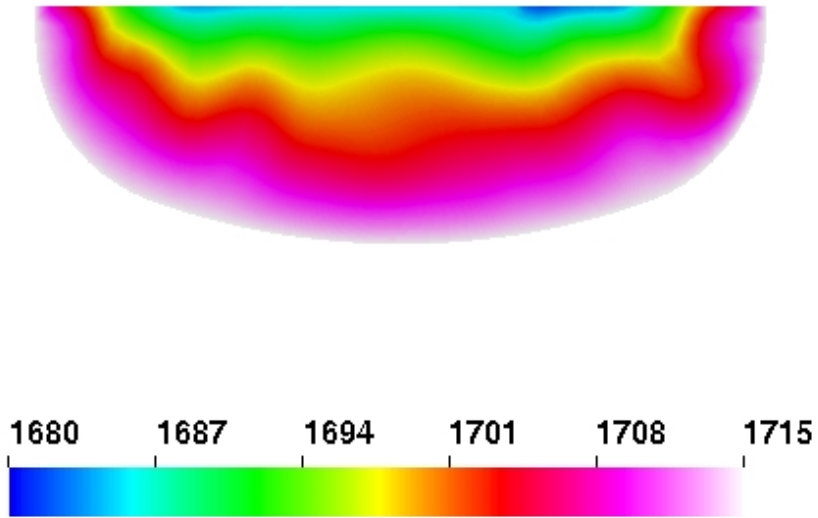


Figure 12: Temperature at the plane $x = 0$ at $t = 150$ s

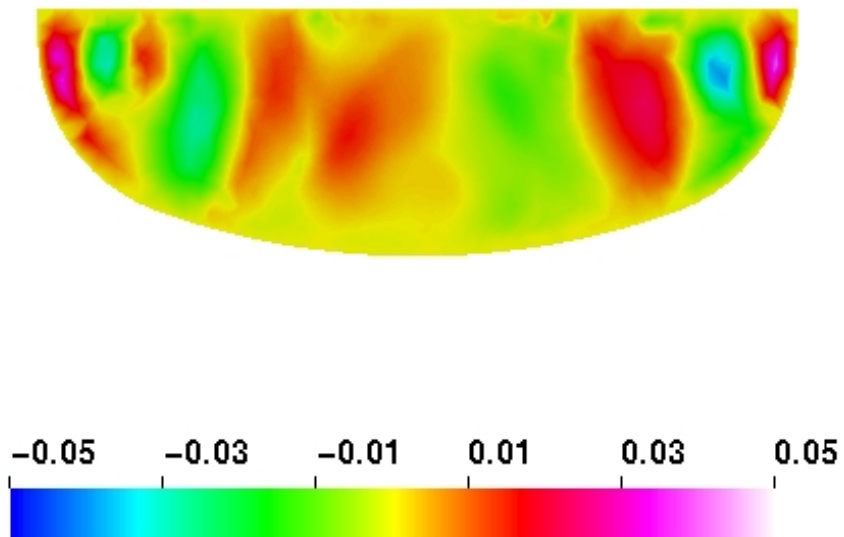


Figure 13: Vertical velocity v_z at the plane $x = 0$ at $t = 150$ s

On the other hand, the numerical solution of the time-dependent and coupled Navier-Stokes and heat equations is computationally very intensive. The

numerical methods and computational power have now reached the point that it is possible to run the simulations on a single powerful processor that has a large memory. Still, a single time step of 1 second real time takes several CPU hours to solve. Therefore, it is not yet reasonable to run the simulations for much longer time periods than we have done as needed for characterization of the quasi-periodic behavior. Likewise, trying out different process parameters or solving the model at different stages of the growth process is out of question. Finally, the melt flow should be coupled to the mathematical model of the CZ growth furnace to obtain more realistic boundary conditions.

In this work we have applied stabilized finite element method in modeling large-scale silicon melt flow in Czochralski crystal growth. The method seems to be very promising to describe complex physical phenomena in the melt.

The process parameters for the large-scale CZ growth system seem to be such that the flow has just entered the quasi-periodic but not yet fully time-dependent and chaotic phase, as the cylindrically symmetric simulation with the real value of the density shows. It is also likely that this is accompanied by the spontaneous break of the axisymmetry, but more simulations on the three-dimensional model are needed to confirm that.

In our future work with the CZ melt flow, we shall try to run the time-dependent three-dimensional simulation with the (more) realistic process parameters. This would require finding an iterative solver and a preconditioner that work for the case. It may also require using a parallelized solver. We have also plans the study the melt flow fluctuations that influence the crystal properties.

On other aspect of the CZ growth, we will model the coupled magnetohydrodynamical system describing the MCZ growth. We have also plans to couple the melt flow to the “global” model.

5 Acknowledgments

This work has been supported by Okmetic Ltd. and Tekes, the National Technology Agency. The authors would like to acknowledge the Center for Scientific Computing in Finland for supercomputer resources.

References

- [1] P.A. Sackinger, R.A. Brown, A Finite Element Method for Analysis of Fluid Flow, Heat Transfer and Free Interfaces in Czochralski Growth, *International Journal for Numerical Methods in Fluids* **Vol. 9** (1989) 453–492
- [2] M. Watanabe, M. Eguchi, K. Kakimoto, T. Hibiya, Double-beam X-ray Radiography System for Three-dimensional Flow Visualization of Molten Silicon Convection, *J. Crystal Growth* **133** (1993) 23–28

- [3] F. Dupret, P. Nicodeme, Y. Ryckmans, P. Wouters, M.J. Crochet, Global Modelling of Heat Transfer in Crystal Growth Furnaces, *Int. J. Heat Mass Transfer* **33** (1990) 1849
- [4] J. Järvinen, Mathematical Modeling and Numerical Simulation of Czochralski Silicon Crystal Growth, *Ph.D. Thesis, University of Jyväskylä, Finland* (1996)
- [5] A. Anselmo, V. Prasad, J. Koziol, K.P. Gupta, Numerical and Experimental Study of a Solid Pellet Feed Continuous Czochralski Growth Process for Silicon Single Crystals, *J. Crystal Growth* **134** (1993) 116–139
- [6] Y. Ryckmans, P. Nicodème, F. Dupret, Numerical Simulation of Crystal Growth: Influence of Melt Convection on Global Heat Transfer and Interface Shape, *J. Crystal Growth* **99** (1990) 702–706
- [7] K. Kakimoto, M. Watanabe, M. Eguchi, T. Hibiya, Flow Instability of the Melt During Czochralski Si Crystal Growth: Dependence on Growth Conditions; a Numerical Simulation Study, *J. Crystal Growth* **139** (1994) 197–205
- [8] Q. Xiao, J.J. Derby, Three-dimensional Melt Flows in Czochralski Oxide Growth: High-resolution, Massively Parallel, Finite Element Computations, *J. Crystal Growth* **152** (1995) 169–181
- [9] K. Kakimoto, P. Nicodème, M. Lecomte, F. Dupret, M.J. Crochet, Numerical Simulation of Molten Silicon Flow; Comparison with Experiments, *J. Crystal Growth* **114** (1991) 715–725
- [10] L.P. Franca, S.L. Frey, T.J.R. Hughes, Stabilized Finite Element Methods: I. Application to the Advective-Diffusive Model, *Computer methods in Applied Mechanics and Engineering* **95** (1992) 253–276
- [11] L.P. Franca, S.L. Frey, Stabilized Finite Element Methods: II. The Incompressible Navier-Stokes Equations, *Computer methods in Applied Mechanics and Engineering* **99** (1992) 209–233
- [12] J. Järvinen, J. Ruokolainen, V. Savolainen, O. Anttila, A Stabilized Finite Element Analysis for Czochralski Silicon Melt Flow, *Proc. for Mathematics In Applications* (25.-28.8.1999, Novosibirsk)
- [13] J. Järvinen, J. Ruokolainen, V. Savolainen, J. Hokkanen *Czochralski Silicon Melt Flow* (video animation, 2000)